Article

Matching and Evaluating Free-form Linear Features for Georeferencing Space-borne SAR Imagery

Dimitra Vassilaki, Athens, Greece

Summary: In this paper, 3D free-form linear features are used as ground control information for the computation of the transformation from 3D object space to the 2D SAR image space. This is now feasible thanks to the high resolution imaging capabilities of contemporary satellite SAR sensors which allow the identification of detailed structures. The computation of the transformation parameters is based on a newly introduced general iterative closest point (ICP) based method for single free-form linear feature pair matching, extended to simultaneously match multiple pairs of them. The proposed method is tested with the georeferencing of a whole TerraSAR-X image. Linear features are shown to be a reliable form of ground control information.

Zusammenfassung: *Matching und Evaluation von Freiform-Linien als Passinformation zur Georeferenzierung von satellitengestützten SAR-Bildern.* In diesem Beitrag werden 3D Freiform-Linien als Passinformation für die Berechnung der Parameter zur Transformation vom 3D-Objektraum in den 2D SAR-Bildraum verwendet. Dies ist dank hoch auflösender moderner SAR Satellitenradarsensoren möglich geworden, die eine Identifizierung detaillierter Strukturen erlauben. Die Berechnung der Transformationsparameter basiert auf einer neu eingeführten Methode, welche eine Verallgemeinerung des Iterative Closest Point-Algorithmus (ICP) zur Zuordnung von einzelnen Paaren von Freiform-Linien darstellt und eine gleichzeitige Identifikation und Zuordnung mehrerer solcher Paare erlaubt. Die vorgeschlagene Methode wird an Hand der Georeferenzierung eines TerraSAR-X-Bildes getestet. Die Linien erwiesen sich dabei als eine zuverlässige Form der Passinformation.

1 Introduction

The fine resolution imaging capability of the modern, state-of-the-art, spaceborne SAR sensors makes feasible the identification of certain details on the Earth's surface such as roads and buildings. This was hard or even impossible with the previous generation of SAR images (Eineder et al. 2009). Modern satellite SAR sensors such as TerraSAR-X collect images that are delivered with an absolute geolocation accuracy of 1–2 m (Roth et al. 2004, Bresnahan 2009). However, the identification of salient characteristic points such as road intersections and building corners is still an ambiguous process, due to the inherently speckled and fuzzy nature of SAR images, the severe distortions inherited from the imag-

ing geometry and the absence of true colour. This is not necessarily a drawback for the SAR images; contemporary SAR sensors may not need control information for orientation processes due to accurate orbit data (Vassilaki et al. 2011a). It is more a problem of the co-processing (combined/synergistic use) of slant range (not geometrically corrected) SAR data with heterogeneous (multimodal and multitemporal) remote sensing and geospatial data, in the sense of identifying salient points to correlate the other data with SAR. The concept of co-processing SAR data with other data types is of growing significance (Sörgel et al. 2008, Wegner et al. 2009, Suri & Reinartz 2010, Vassilaki et al. 2011b, Wegner et al. 2011, Reinartz et al. 2011). There is a worldwide abundance of readily available geospatial informa-

tion as other type of data. Moreover, optical images are of well-established use and of more descriptive nature as they are closer to the human eye perception. On the other hand, SAR is an all-weather, day and night sensor, offering information about the properties of the targets, their 3D geometry and their evolution over time, which complements information found in other data types.

In order to work around the ambiguous identification of salient points on the fuzzy and speckled SAR images, linear features such as road edges and building outlines are investigated as an alternative way to provide ground control information (GCI). The concept of using non salient point GCI for the geometric co-processing of SAR images with other, heterogeneous, remote sensing and geospatial data is relatively new, as the identification of details was hard with previous generations of SAR images; Dare & Dowman (2001) and Karjalainen (2007) used water body boundaries, which are effectively 2D, for registration problems and Zalmanson et al. (2004) attempted an introductory research on a more general 3D approach using parametric curves, with no applications or results. In this paper the georeferencing of TerraSAR-X images is done with a newly introduced ICP-based free-form linear features (FFLFs) matching method (Vassilaki et al. 2008). FFLFs are 2D or 3D linear features of arbitrary geometry, such as road edges and building outlines, defined by nodes of no regularity which are joined by a function of arbitrary type (Vassilaki et al. 2012). In this paper the method is extended to match networks of FFLFs of different dimensionality (3D-2D). The method is applied to the georeferencing of a whole TerraSAR-X image; a network of 3D FFLFs is used as GCI or ground control linear features (GCLFs) in order to compute the parameters of the transformation from 3D object space to 2D SAR image space.

2 Problem Formulation

A SAR image is a 2D projection (x,y) of the 3D object space (X,Y,Z). The georeferencing process recovers the imaging geometry of the sensor at the time of acquisition, by the computation of the parameters of the transforma-

tion. Transformations are generally classified into empirical models and into physical sensor models (Toutin 2004). Examples of empirical models are polynomial functions (PFs) and rational polynomial functions (RPFs), while physical sensor models are sensor dependent rigorous mathematical functions. In this paper the georeferencing is computed by using PFs and RPFs as transformation models, and the results are compared to those achieved using the physical model of Vassilaki et al. (2011a). Although not widely adopted for SAR images (Toutin 2004, Dowmann & Dolloff 2000), the use of empirical sensor models is still geometrically meaningful as it was recently explained by Zhang et al. (2011). Traditionally the computation of the transformation parameters, either empirical or physical, requires salient points with known 3D object-space and 2D image-space coordinates (ground control points, GCPs).

In this paper the georeferencing parameters are computed using FFLFs with known 3D object-space and 2D image-space coordinates (GCLFs). In contrast to salient points, the 3D information and the 2D information are in the form of a pair of two distinct heterogeneous FFLFs defined by their nodes (measured points). These nodes may vary widely as they are produced using different processes. Even though a corresponding pair of FFLFs represents the same physical feature, generally no two nodes of the FFLFs correspond to the same physical point (Vassilaki et al. 2012). Homologous point pairs have to be computed (matched). The matching is complicated by the fact that the two FFLFs are of different dimensionality. Furthermore, a single pair of FFLFs may not represent the entire dataset, as it may be confined to a small region of the data. In this case, multiple pairs or a network of corresponding FFLFs are required. The network of FFLFs increases the robustness but it introduces problems such as the FFLFs correspondence and simultaneous matching.

3 Overview of the Method

A novel method based on the iterative closest point (ICP) algorithm (Besl & McKay 1992, Zhang 1994) is used for accurate and robust

global matching of heterogeneous FFLFs. The method was initially introduced in VASSILAKI et al. (2008) in order to match 2D heterogeneous FFLFs with a rigid transformation. It was further expanded in order to match FFLFs of different dimensionality (2D-3D) with non-rigid projective transformation and it is fully documented in VASSILAKI et al. (2012). For efficiency convenience and user friendliness the method has been incorporated into ThanCAD (STAMOS 2007), an open-source CAD.

The matching of two FFLFs of the same dimensionality (2D-2D, 3D-3D) is done by an iterative process of determining closest point pairs between the two FFLFs and then using them to compute the transformation parameters by least squares adjustment (LSA). Closest point pairs are computed by splitting a FFLF to a large set of consecutive interpolated points, each one very close to its previous and its next point. Then, the distances of all these points to a node of the other FFLF are computed; the closest points between the two FFLFs are the points with the smallest distances (VASSILAKI et al. 2008). This process may be computationally expensive but it is doable with modern computers, and it is relatively easy to speed it up with a divide-and-conquer approach. Further acceleration can be achieved by parallel computing. In the case of FFLFs of different dimensionality (3D-2D) the 3D nodes of the 3D FFLF are projected to the 2D image space using an initial or previous approximation of the transformation parameters, saving the association of each 3D node and its 2D projection. Closest points are computed as in the 2D-2D case, they are converted to 3D-2D pairs through the saved association, and they are used to compute the projection parameters by LSA. Detailed description of the 3D-2D case can be found in VASSILAKI et al. (2009b).

The ICP algorithm needs a good initial approximation to converge, which means that the two FFLFs must be close enough to each other. Automatic pre-alignment is done using the rigid similarity transformation computed exploiting physical properties of the two FFLFs, or using the non-rigid first order polynomial (affine) transformation computed exploiting characteristic statistical properties of the FFLFs (VASSILAKI et al. 2012).

In the case of networks of FFLFs of the same dimensionality (2D-2D, 3D-3D), the correspondences of FFLFs must be established. Assuming that the two datasets are initially pre-aligned, a FFLF of the first dataset corresponds to the FFLF of the other dataset which is "closest" to it. However, the definition of "closest" is ambiguous for a FFLF which may span many other FFLFs. Different nodes of the same FFLF may be closest to nodes of different FFLFs. VASSILAKI et al. (2009a) introduced the term "distance" as an integral measure of how far or how different two FFLFs are. The pair of FFLFs which have the smallest "distance" are assumed to correspond to each other. Four candidates for the "distance" measure were suggested: the Euclidean distance between characteristic homologous points, namely the first nodes ($d1$), the last nodes (dN), or the centroids (d), and the absolute difference of the FFLFs lengths (ΔS). For robustness, the biggest of these four values can be used as the "distance" of the FFLFs. In the very unlikely case that the "distance" is ambiguous (almost the same) for two or more pairs of FFLFs, application of the full ICP can be used to determine which FFLFs correspond. ICP is the best and more robust approach, but it is very time consuming and should be avoided if possible. VASSILAKI et al. (2009a) assumes global matching, implying that the number of FFLFs of each network is the same (N:N matching). The method, however, has partial matching capabilities which can be further exploited in future research. If the number of FFLFs of the two networks is different (N:M matching, N>M), the method finds the "closest" pair of FFLFs, marks these FFLFs as corresponding pair of FFLFs, and continues the same process for the remaining FFLFs (N-1:M-1 matching). In the end N-M single FFLFs are left, which are effectively ignored. The method proceeds with an ICP step, it brings the FFLFs even closer and it then re-evaluates the correspondence, as the "distance" between any pair of FFLFs is obviously changed. Furthermore, ICP automatically rejects two unrelated FFLFs marked to correspond if they do not overlap (VASSILAKI et al. 2012).

All the FFLFs of a network share a common transformation. In order to compute the

common transformation, LSA is applied to all the pairs of FFLFs simultaneously. The equations produced by the homologous points of all pairs of FFLFs are assembled into the same LSA matrices. The LSA computes the transformation which best fits all the pairs of FFLFs. The computed transformation brings the FFLFs closer together, and thus the correspondences are re-evaluated, in case that the previous, poorer, transformation led to a few false correspondences.

4   Matching 3D-2D Networks of FFLFs

In this paper, the method is extended to match networks of FFLFs of different dimensionality (3D-2D). VASSILAKI et al. (2009a) used manually pre-aligned datasets, which in the case of 3D-2D is rather difficult as the varying Z coordinate of the 3D FFLFs and the geometrical distortions on the SAR image (2D FFLFs) makes their shapes incompatible. Manual move, scale and rotate operations, typically provided by CAD software, are not enough to cancel the elongated nature of the SAR projection. Instead, the 3D FFLFs must be projected to the image space of the 2D FFLFs using a good approximation of the unknown transformation parameters. Since all pairs of FFLFs share the same transformation, a good approximation of the projection of a single pair of FFLFs, automatically computed (VASSILAKI et al. 2012), can be used to project the 3D FFLFs network to the 2D image space, bringing the datasets close together. The 2D-2D correspondences of FFLFs are then established as outlined in the previous section (VASSILAKI et al. 2009a). The correspondence of the single pair of FFLFs is chosen manually by the user, so that in this sense the datasets are manually pre-aligned. However, apart from this, the procedure is fully automated.

5   Design of Tests, Datasets and Results

The experiments were designed to test both the robustness and the accuracy of the method. In the group "A" tests, the georeferencing

of a TerraSAR-X image is done using GCI extracted from a 40 years old map. In the group "B" tests, the georeferencing of the same TerraSAR-X image is done using recently captured optical aerial images. Group A is a "crash test" of the proposed method and it may be of practical use in urgent situations when there is no time to collect up-to-date GCI (a day is enough for a satellite scene under the current method). Group B, where the datasets are compatible in terms of time, is a contribution to the operational georeferencing of TerraSAR-X images and their combined use with optical images. Each group of experiments contains tests corresponding to four distinct projection models:

- first order 3D PFs with 8 unknown parameters (3D affine model)

$$x = a_1 X + a_2 Y + a_3 Z + a_4$$
$$y = b_1 X + b_2 Y + b_3 Z + b_4 \qquad (1)$$

- second order 3D PFs (TOUTIN 2004) with 16 unknown parameters

$$x = a_1 X + a_2 Y + a_3 Z + a_4 + a_5 X^2 + a_6 Y^2$$
$$\quad + a_7 Z^2 + a_8 XY$$

$$y = b_1 X + b_2 Y + b_3 Z + b_4 + b_5 X^2 + b_6 Y^2$$
$$\quad + b_7 Z^2 + b_8 XY \qquad (2)$$

- 3D Direct Linear Transform (DLT) with 11 unknown parameters

$$x = \frac{a_1 X + a_2 Y + a_3 Z + a_4}{c_1 X + c_2 Y + c_3 Z + 1}$$

$$y = \frac{b_1 X + b_2 Y + b_3 Z + b_4}{c_1 X + c_2 Y + c_3 Z + 1} \qquad (3)$$

- 3D RPFs with 14 unknown parameters

$$x = \frac{a_1 X + a_2 Y + a_3 Z + a_4}{c_1 X + c_2 Y + c_3 Z + 1}$$

$$y = \frac{b_1 X + b_2 Y + b_3 Z + b_4}{d_1 X + d_2 Y + d_3 Z + 1} \qquad (4)$$

where X,Y,Z are the object coordinates and x,y are the SAR image space coordinates (slant range and azimuth, respectively).

The study area is a sub-urban area in the greater north-eastern region of Athens, Greece. It has steep mountainous terrain with an average elevation of 270 m and it is generally covered by sparse vegetation. It also

includes two small urban regions. The data used (Fig. 1) are a) a TerraSAR-X image, b) an old medium scale topographic map and c) a recent medium-scale optical orthoimage with the corresponding digital terrain model (DTM) (Fig. 1). The TerraSAR-X image is a single look slant range (SSC) imaging product captured in 2009 with the experimental 300 MHz high resolution spotlight (HS) imaging mode. The whole image, which covers an area of about 50 km^2 (5 km x 10 km), was used. The polarisation is HH and the scene centre incidence angle is 53°. The projected spacing values for range (ps$_{Rg}$) and azimuth (ps$_{Az}$) are 0.45 m and 0.87 m, respectively. The medium-scale old topographic map was in analogue form at a scale of 1:5000 and it was compiled by stereo-restitution from aerial photos, captured in 1970. The map was converted to digital form by scanning and digitizing; the contour lines of the map were converted to a DTM. The relative planar accuracy of the map is estimated at 1.5 m (σ_{Pl}). The vertical contour interval is 4 m and the relative vertical accuracy is estimated at 2 m (σ_Z). The absolute planar accuracy is estimated at 2.5 m (σ_{Pl}) and the vertical one at 4 m (σ_Z). The map is part of a series which cover the whole territory of Greece. They are readily available and they cost much less than a GPS survey. The area under study changed widely during

the 40 years between the two data collection phases (2009 and 1970). The area used to be an agricultural area but now exhibits a great variety of land uses, as it serves as a holiday resort near Athens. The map and the SAR image share few common features, as is the case in virtually all multitemporal datasets. Most of these common features are roads which, unfortunately, evolve through time. Many sections of the roads have changed considerably during the 40 years between data acquisitions, as it is shown in the next paragraphs. The maps are topographic maps (not illustration or small scale maps) of scale 1:5000 and thus there are no (significant) generalizations. Furthermore, most of the used roads are more than 6 m wide, which means that their width is over 1 mm in the map, and thus, the roads are clearly visible. The medium-scale optical orthoimage and the corresponding DTM were available with pixel sizes of 0.5 m and 5 m, respectively. The orthoimage was produced from aerial images collected in 2008. The orthoimage and the corresponding DTM are of the same nominal accuracy as the paper map, probably because they were also compiled to meet the specifications for mapping at a scale of 1:5000.

The 3D error of the datasets must be expressed in terms of the 2D SAR image space, since this paper deals with the projection (in
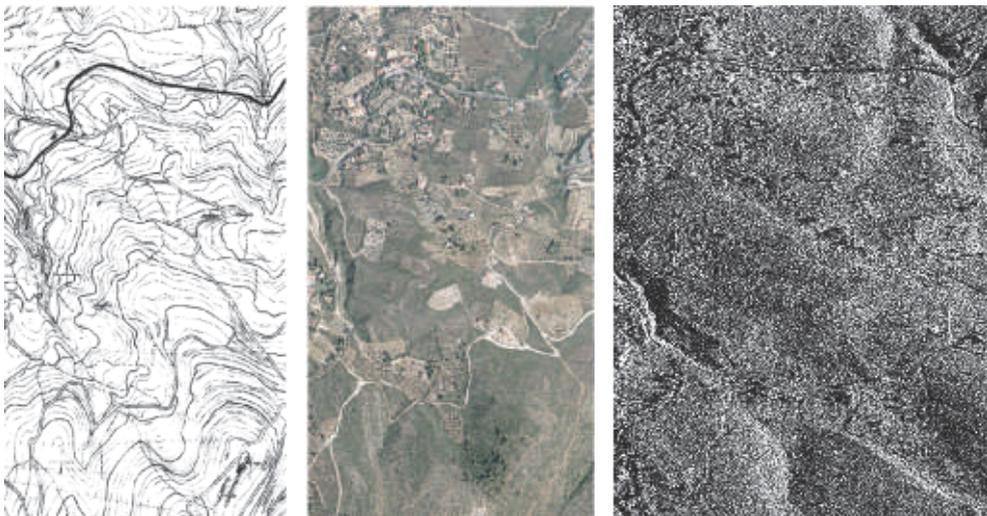
Fig. 1: Datasets: old map (left), orthoimage (middle), SAR image (right).

the mathematical sense) of the 3D object space to the 2D SAR image space. The error propagation of the object space to the SAR image space is given in Appendix 1. The planar relative error (σ_{Pl} = 1.5 m) and the vertical relative error (σ_Z = 2 m) of the 3D object space map are propagated to 1.4 m in the SAR range direction ($\sigma_{Rg,pix}$) and 0.9 m in the SAR azimuth direction ($\sigma_{Az,pix}$), while the planar absolute error (σ_{Pl} = 2.5 m) and the absolute vertical error (σ_Z = 4 m) are propagated to 2.7 m in the SAR range direction ($\sigma_{Rg,pix}$) and 1.7 m in the

SAR azimuth direction ($\sigma_{Az,pix}$). These values are valid for the specific SAR image of this paper and are used later for evaluation purposes.

In all tests, the extraction of 2D road edges was done manually by digitizing the lines in the map or in the optical image and in the SAR image. Most of the roads digitized are paved, as they appear better in the SAR images. The road centre lines were obtained from the edges using a skeletonization technique based on the method proposed in VASSILAKI et al. (2012). The road centre line is preferred to
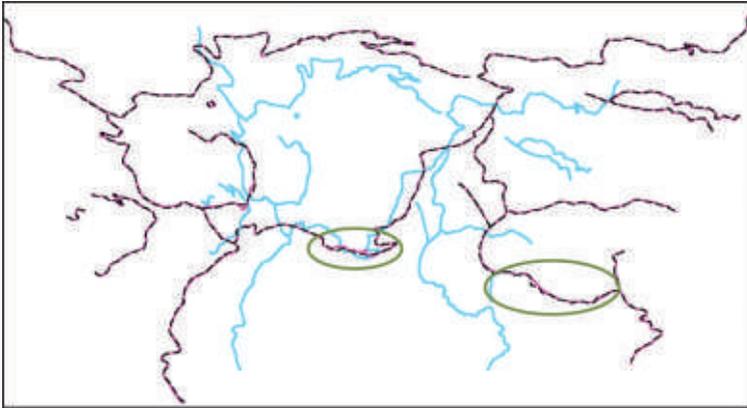
Fig. 2: Matching results of Test A0. 3D GCLFs extracted from the old map (cyan), 2D GCLFs extracted from the SAR image (magenta), matched projection of the 3D GCLFs (black dashed). Fig. 3 shows the road sections inside the green ellipses in a magnified version (GCLF = ground control linear features).
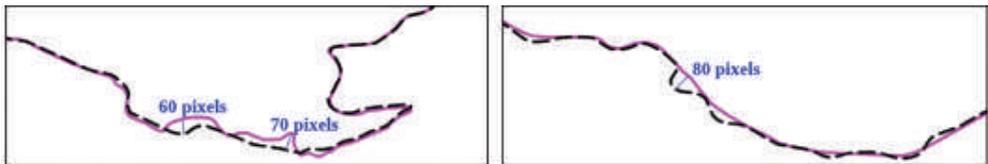
Fig. 3: Test A0: Road sections with wide temporal changes. 2D GCLFs (magenta), matched projection of the 3D GCLFs (black dashed).
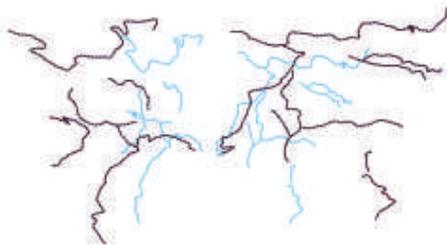
Fig. 4: Matching results of Test A1. GCLFs with wide temporal changes are excluded.
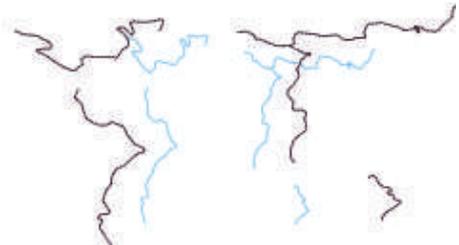
Fig. 5: Matching results of Test A2. Only few GCLFs are used.
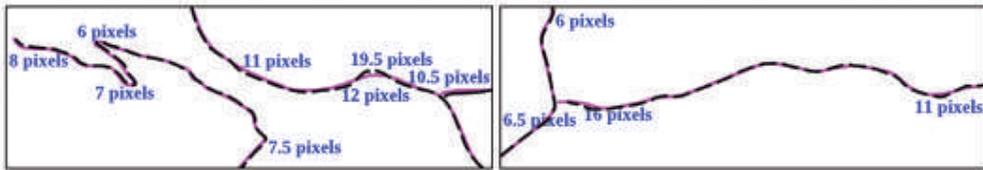
Fig. 6: Test A1: Road sections with temporal changes. 2D GCLFs (magenta), matched projection of the 3D GCLFs (black dashed).
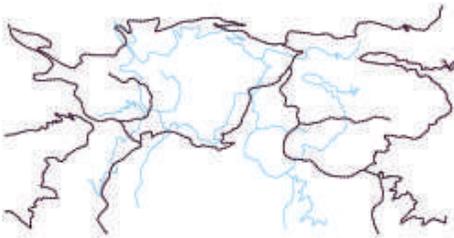
Fig. 7: Matching results of Test B1. The 3D GCLFs are extracted from a recent orthoimage.
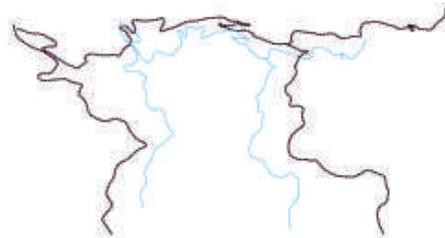
Fig. 8: Matching results of Test B2. Only few GCLFs are used.

road edges as control FFLF, because it is more accurate than the edges and it fully represents the geometry of the road. For all the tests, a preliminary georeferencing was computed using a single pair of corresponding FFLFs that was identified manually. The computed transformation parameters were used to bring the network of FFLFs close together.

In tests A, the length of the road centre lines varies from a few hundred meters to 8.5 km (Fig. 2 and Figs. 4–5). The height profiles of the road centre line are in general rough, due to the scale of the map and the fact that the map does not have elevation information along the surface of the road. The centre line elevation, interpolated in the DTM, was determined by the heights of the surrounding terrain. Three different cases were tested. In the first case (A0) the centre lines of 14 roads were used as ground control linear features (GCLFs). The whole lengths of the roads were used, regardless of the temporal changes that were identified. In the second case (A1) the same 14 centre lines as in (A0) were used, but the sections of the roads which exhibited large temporal changes were eliminated manually as identified by (A0). In the third case (A2) the centre lines of 4 roads, which span the whole scene of the SAR image, were used as GCLFs. The matching results are shown in Fig. 2 and Figs.

4–5. The 3D GCLFs which were extracted from the map appear in cyan colour, the SAR 2D GCLFs appear in magenta colour, and the matched projection of the 3D GCLFs using the proposed method appear with a black dashed line. It must be noted that the coordinates of 3D GCLFs (cyan) and 2D GCLFs (magenta) were too different to fit into the same figure and thus the 3D GCLFS are shown scaled/translated for illustration purposes. In Fig. 3 characteristic sections of the roads with wide temporal changes are presented for case A0. In Fig. 6 characteristic sections with temporal changes are presented for case A1.

In tests B, the length of the road centre lines varies from 1.5 to 12 km (Figs. 7–8). Two different cases were tested. In the first case (B1) the centre lines of 9 roads were used as GCLFs. In the second case (B2) the centre lines of 3 roads, which span the whole scene of the SAR image, were used as GCLFs. The matching results are shown in Figs. 7–8.

6 Validation, Evaluation and Discussion of the Results

The accuracy of the computed georeferencing was checked with independent check points (CPs). In test A, 16 CPs were extracted from

the medium scale old map and were also identified in the SAR image. Fig. 9 shows the distribution of the CPs and Tab. 1 shows the RMSE (root-mean-square error) (in m) for the four computed transformation models (1–4). The RMSE is the root-mean-squared differences between the image coordinates of the CPs and the image coordinates of the CPs computed from their object coordinates using the computed transformation model. It is noticeable that the RMSE of the CPs is almost the same regardless of the transformation model used. The differences (1.1 m at most) are not statistically significant as they are less than the accuracy of the maps (1.4 m in range and 0.9 m in azimuth directions) and the uncertainty of the point location on the SAR image is larger than 1 pixel. It is also noticeable that the method is insensitive to temporal changes, given the abundance of GCLFs found in all cases (A0,

A1 and A2). The method manages to match robustly and efficiently data which contain sections with gross temporal changes, producing low RMSE. In the first case (A0) the GCLFs contain gross errors in various segments with temporal changes, but they cancel out. In fact, the method can also be used to identify the erroneous segments and exclude them from the matching, but this remains a subject of future research. The erroneous segments were removed manually in the second case (A1). After running tests A0, the distance of some segments of the matched roads were far larger than the rest. The length of these segments was small compared to the length of the roads. If the difference was greater than a threshold (more than 3 times the average difference of the rest) and the length of the segment was greater than 5 times this threshold, the segment was excluded manually. Case A1 tends
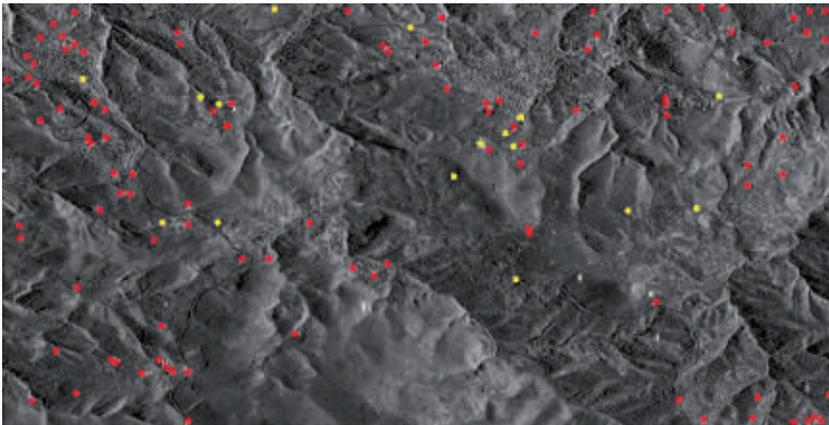
Fig. 9: The CP distribution used for tests A (yellow) and B (red), shown on the SAR image.

Tab. 1: RMSE of the transformation models using CPs (m). The error is dominated by the a-priori error of the GCI and/or CPs (GCI = ground control information, GCLF see Fig. 2).

Test	GCI: GCLFs								GCI: none	
	1st order PFs		2nd order PFs		DLT		RPFs		Physical model	
	dRg	dAz	dRg	dAz	dRg	dAz	dRg	dAz	dRg	dAz
A0	1.9	3.4	2.4	4.1	2.6	3.7	2.3	4.5	2.4	3.5
A1	1.8	3.1	2.2	3.2	1.9	3.2	2.0	3.3		
A2	2.1	3.9	2.2	4.1	1.8	4.1	2.0	3.4		
B1	1.3	2.4	1.1	2.9	1.3	2.5	1.2	2.7	2.3	2.6
B2	1.3	2.6	1.2	3.5	1.5	2.8	1.3	2.9		

to give the best RMSE. In the last case (A2) the number of GCLFs is only 4, but they cover adequately the whole scene, and give almost the same RMSE as (A0).

In tests B, 108 CPs were extracted from the optical image and the corresponding DTM and were also identified on the SAR image. The abundance of salient points which can be identified both on the optical and the SAR image offered the opportunity to collect a great number of CPs in order to improve the reliability. Features such as roads, pools, big buildings and field boundaries are identified clearly on both image types. Metallic objects appear brightly on the SAR image but it was impossible to identify them on the optical image. Built-up areas appear clearly in the optical image, but their interpretation in the SAR image was hard due to the layover and shadow effects. The elevation of features above the terrain surface could not be determined as only ground elevation information was available. Thus, the majority of CPs are corners of pools, field boundaries, and characteristic points of roads. Fig. 9 shows the distribution of the CPs, Fig. 10 shows some of the CPs in detail and Tab. 1 shows the RMSE (in m) for the four computed transformation models (1–4). The conclusions of tests A are verified in tests B: 1) the RMSE of the CPs is almost the same regardless of the transformation model used and 2) the RMSE is not sensitive to the number of GCLFs, if they cover adequately the scene. It

should also be noted that the RMSE is very close to the relative accuracy of the orthoimage and the corresponding DTM, computed in Appendix 1 (1.4 m and 0.9 m in the SAR range and azimuth directions, respectively).

The results computed with the present method (GCLFs) tend to be of better quality than those computed by salient point based approaches. In VASSILAKI & IOANNIDIS (2010) a terrain dependent approach was applied to the datasets of tests A using the 3D DLT (11 parameters) and the 1st order 3D RPF (14 parameters) transformations. The RMSE of independent CPs was about 3.2 m in range and about 3.0 m in azimuth direction. About the same results were later achieved by CRESPI et al. (2010), who used a terrain independent approach to georeference a SpotLight COSMO-SkyMed image, using 3rd order 3D RPFs (78 parameters, 20 of which proved to be statistically significant). In NONAKA et al. (2008) a digital map at a scale of 1:2500 was used in order to evaluate the accuracy of the orthorectified EEC SpotLight TerraSAR-X products. The accuracy revealed to be better than 5 m in a flat area while it degraded to more than 10 m in mountainous areas.

Comparing the RMSE computed with the present method (GCLFs with empirical models) to those computed with the SAR physical model (without GCI), one might erroneously conclude that the present method is better. However, in both cases the error of the GCI
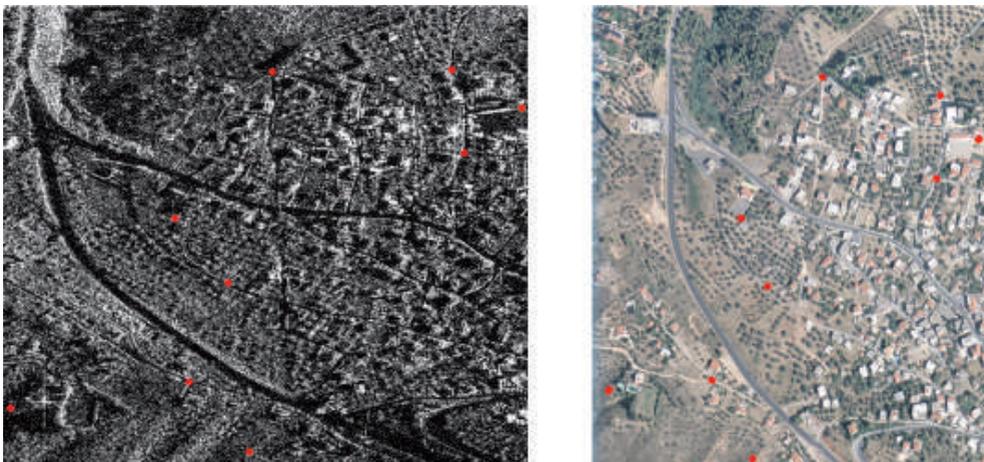
Fig. 10: Some of the CPs used for test B, shown on the SAR (left) and optical (right) image.

and/or the CPs (map, orthoimage, uncertainty of the point location in the SAR image) dominates the (much smaller) error of the sensor. Furthermore, the empirical models reflect the relative accuracy of the GCI, while the physical model reflects the absolute accuracy of the GCI which is worse than the relative one. In VASSILAKI et al. (2011a), where the physical model was used with the datasets of tests A, the RMSE of the independent CPs is 2.4 m in range and 3.5 m in the azimuth direction. The absolute accuracy of the map, computed in Appendix 1, was 2.7 m and 1.7 m in the SAR range and azimuth directions, respectively. The RMSE in range is close to the one to be expected, but in azimuth it is somewhat larger. The overall 2D errors (geometric mean of range and azimuth), which are 4.2 m and 3.2 m for our results and the expected accuracy, respectively, are also relatively close. The relatively large RMSE values in azimuth require further investigations. In test B the RMSE of the 108 CPs computed using the physical model is 2.3 m in range and 2.6 m in the azimuth direction. This is close to the absolute accuracy of the orthoimage and the corresponding DTM (the same as in test A) in range and also closer in azimuth than in test A. Again, the overall 2D error is close to the one expected (an overall RMSE of 3.4 m vs. an expected accuracy of 3.2 m). Thus, the results computed with the present method are of the same quality as the ones computed by the physical model without GCI.

7 Conclusions

The pixel location accuracy of TerraSAR-X images has been validated in the past by its operator and by independent researchers, with dedicated projects which demand the installation of corner reflectors on strategic places on the Earth's surface and the acquisition of datasets appropriate for this purpose. Although the accuracy was proven to be well below 1 m, the use of corner reflectors either as control or as check points is generally not desirable and/or feasible in everyday operational cases of research and practice, even more so in emergency situations. The objective of this paper was to evaluate the performance of lin-

ear features as GCI for the operational georeferencing of TerraSAR-X images. Research conducted so far, in a sub-urban mountainous area, shows that contemporary satellite SAR sensors and the proposed method is promising with respect to robustness and accuracy: 1) linear features with large temporal changes, due to the 40 years time interval between the data acquisitions, are matched robustly and lead to a reliable recovery of the imaging geometry of the sensor (RMSE on independent CPs: 1.9 m in range and 3.2 m in azimuth), 2) linear features extracted from an optical image and the corresponding DTM are a reliable form of GCI (RMSE on independent CPs: 1.3 m in range and 2.5 m in azimuth).

The RMSE differences between the models (PFs, DLT, RPFs) are inconclusive as all models approach the accuracy of the map. The use of more accurate check points is needed for further evaluation. Automated extraction of the linear features is also expected to serve the goal of further refinement. However the latter will be not a trivial task because the road surfaces may be paved or not, and the material of the pavement may vary across a road's surface due to additional lanes. E.g. the deceleration lane may be paved, semi-paved or not paved at all. These facts differentiate the appearance of a road surfaces in the optical and the SAR images and make it hard to identify the differences, even for the human eye.

Two issues revealed in this paper need further research: 1) the good performance of simple transformations such as the first order PFs when linear features are used as GCI, and 2) the impact of the absolute and relative error of the ground information (CPs, GCPs and GCLFs) on the performance of GCI-based methods as compared to the physical sensor model without GCI.

Appendix 1: Error Propagation from Object Space to SAR Image Space

A point P(X,Y,Z) measured on a map contains a planar error σ_{Pl} and a vertical error σ_Z inherited from the accuracy of the map. There is no reason to assume that the σ_{Pl} error is different in any particular direction so that $\sigma_X = \sigma_Y = \sigma_{PL} / \sqrt{2}$. The directions x, y

are taken as the range and azimuth directions of the SAR sensor, respectively. The error σ_Y (m) is also the expected SAR image error in the azimuth direction of the SAR image. The σ_Z, σ_X errors lead to SAR image error in the range direction, which is more complicated due to the slant range geometry of the SAR sensor. The slant distance (S_D) from the sensor (X_0,Y_0,Z_0) to the point (X,Y,Z) is given by (5) where $k = Z/Z_0 \ll 1$ and φ is the mean incidence angle of all points in the SAR image. The error of the slant distance is then computed by (6). As the pixel spacing is different in the range (ps_{Rg}) and azimuth (ps_{Az}) direction of the SAR image, the error in pixels is computed by (7).

Acknowledgements

$$S_D = f(Z,X) = \sqrt{(Z_0 - Z)^2 + (X_0 - X)^2} \approx \sqrt{(Z_0 - Z)^2 + Z_0^2 \tan^2 \varphi} = Z_0\sqrt{(1-k)^2 + \tan^2 \varphi} \tag{5}$$

$$\sigma_{S_D}^2 = (\frac{\partial f}{\partial Z})^2 \sigma_Z^2 + (\frac{\partial f}{\partial X})^2 \sigma_X^2 = \frac{(Z_0 - Z)^2}{(Z_0 - Z)^2 + (X_0 - X)^2}\sigma_Z^2 + \frac{(X_0 - X)^2}{(Z_0 - Z)^2 + (X_0 - X)^2}\sigma_X^2 \approx$$

$$\approx \frac{Z_0^2(1-k)^2}{Z_0^2[(1-k)^2 + \tan^2 \varphi]}\sigma_Z^2 + \frac{Z_0^2 \tan^2 \varphi}{Z_0^2[(1-k)^2 + \tan^2 \varphi]}\sigma_X^2 \approx \frac{1}{1 + \tan^2 \varphi}\sigma_Z^2 + \frac{\tan^2 \varphi}{1 + \tan^2 \varphi}\sigma_X^2$$

$$= \cos^2 \varphi \sigma_Z^2 + \sin^2 \varphi \sigma_X^2 \Rightarrow \sigma_{S_D} \approx \sqrt{\cos^2 \varphi \ \sigma_Z^2 + \sin^2 \varphi \ \sigma_X^2} \tag{6}$$

$$\sigma_{Rg,pix} \approx \frac{1}{ps_{Rg}}\sqrt{\cos^2 \varphi \ \sigma_Z^2 + \sin^2 \varphi \ \sigma_X^2} \qquad \sigma_{Az,pix} \approx \frac{1}{ps_{Az}}\sqrt{\frac{\sigma_{PL}^2}{2}} \tag{7}$$

References

BESL, P.J. & McKAY, N.D., 1992: A Method for Registration of 3-D Shapes. – IEEE Transactions on Pattern Analysis and Machine Intelligence **14** (2): 239–256.

BRESNAHAN, P., 2009: Absolute Geolocation Accuracy Evaluation of TerraSAR-X Spotlight and Stripmap Imagery – Study Results. – Civil Commercial Imagery Evaluation Workshop, 31 March – 2 April, 2009, USGS, Fairfax Virginia, USA.

CRESPI, M., CAPALDO, P., FRATARCANGELI, F., NASCETTI, A. & PIERALICE, F., 2010: DSM generation from very high optical and radar sensors: Problems and potentialities along the road from the 3D geometric modeling to the surface model. – IEEE International Geoscience and Remote Sensing Symposium: 3596–3599.

DARE, P. & DOWMAN, I., 2001: An improved model for automatic feature-based registration of SAR and SPOT images. – ISPRS Journal of Photogrammetry and Remote Sensing **56** (1): 3–28.

DOWMAN, I. & DOLLOFF, J., 2000: An evaluation of rational function for photogrammetric restitution. – International Archives of Photogrammetry and Remote Sensing **33** (B3): 254–266.

EINEDER, M., ADAM, N., BAMLER, R., YAQUE-MARTINEZ, N. & BREIT, H., 2009: Spaceborne Spotlight SAR Interferometry with TerraSAR-X. – IEEE Transactions on Geoscience and Remote Sensing **47** (5): 1524–1535.

KARJALAINEN, M., 2007: Geocoding of synthetic aperture radar images using digital vector maps. – IEEE Geoscience and Remote Sensing Letters **4** (4): 616–620.

NONAKA, T., ISHIZUKA, Y., YAMANE, N., SHIBAYAMA, T., TAKAGISHI, S. & SASAGAWA, T., 2008: Evalua-

tion of the Geometric Accuracy of TerraSAR-X. – International Archives of the Photogrammetry, Remote Sensing and Spatial Information Sciences **37** (B7): 135–140.

REINARTZ, P., MÜLLER, R., SCHWIND, P., SURI, S. & BAMLER, R. 2011: Orthorectification of VHR optical satellite data exploiting the geometric accuracy of TerraSAR-X data. – ISPRS Journal of Photogrammetry and Remote Sensing **66** (1): 124–132.

ROTH, A., HUBER, M. & KOSMANN, D. 2004: Geocoding of TerraSAR-X Data. – International Archives of Photogrammetry, Remote Sensing and Spatial Information Sciences **35** (3): 840–845.

SÖRGEL, U., CADARIO, E., THIELE, A. & THOENNESSEN, U., 2008: Feature Extraction and Visualization of Bridges over Water from high-resolution InSAR Data and one Orthophoto. – IEEE Journal of Selected Topics in Applied Earth Observations and Remote Sensing **1** (2): 147–153.

STAMOS, A.A., 2007: ThanCad: a 2dimensional CAD for engineers. – Europython2007 Conference, Vilnius, Lithuania, http://thancad.sourceforge.net/thancad10.pdf, 11 p. (29.2.2012).

SURI, S. & REINARTZ, P., 2010: Mutual-information-based registration of TerraSAR-X and Ikonos imagery in Urban areas. – IEEE Transactions on Geoscience and Remote Sensing **48** (2): 939–949.

TOUTIN, T., 2004: Review Paper: Geometric processing of remote sensing images: models, algorithms and methods. – International Journal of Remote Sensing **25** (10): 1893–1924.

VASSILAKI, D.I, IOANNIDIS, C. & STAMOS, A.A., 2008: Registration of 2D Free-Form Curves Extracted from High Resolution Imagery using Iterative Closest Point Algorithm. – EARSeL's Workshop on Remote Sensing – New Challenges of High Resolution **2008:** 141–152, Bochum, Germany.

VASSILAKI, D.I., IOANNIDIS, C. & STAMOS, A.A., 2009a: Multitemporal Data Registration through Global Matching of Networks of Free-form Curves. – 2009 FIG Working, Eilat, Israel, cd.

VASSILAKI, D.I., IOANNIDIS, C. & STAMOS, A.A., 2009b: Registration of Unrectified Optical and SAR imagery over Mountainous Areas through Automatic Free-form Features Global Matching. – International Archives of Photogrammetry, Remote Sensing and Spatial Information Sciences **38** (1-4-7/W5): cd.

VASSILAKI, D.I. & IOANNIDIS, C., 2010: Georeference of High Resolution TerraSAR-X Images with RPFs. – 30th EARSeL Symposium Proceedings: 573–580.

VASSILAKI, D.I., IOANNIDIS, C. & STAMOS, A.A., 2011a: Georeference of TerraSAR-X images using Science Orbit Data. – 31st EARSeL Symposium Proceedings: 472–480.

VASSILAKI, D.I., IOANNIDIS, C. & STAMOS, A.A., 2011b: Fusion of optical and SAR images in slant range SAR geometry. – 31st EARSeL Symposium Proceedings: 552–560.

VASSILAKI, D.I., IOANNIDIS, C. & STAMOS, A.A., 2012: Automatic ICP-based global matching of freeform linear features. – Photogrammetric Record, doi: 10.1111/j.1477-9730.2012.x.

WEGNER, J.D., AUER, S. & SÖRGEL, U., 2009: Accuracy assessment of building height estimation from high resolution optical image combined with a simulated SAR image. – International Archives of Photogrammetry, Remote Sensing and Spatial Information Sciences **38** (1-4-7/WS): cd.

WEGNER, J.D., HÄNSCH, R., THIELE, A. & SÖRGEL, U., 2011: Building Detection From One Orthophoto and High-Resolution InSAR Data Using Conditional Random Fields. – IEEE Journal of selected topics in applied Earth Observations and Remote Sensing **4** (1): 83–91.

ZALMANSON, G.H., DOYTSHER, Y. & SCHENK, T., 2004: Towards a new paradigm for registration of SAR images using linear features. – International Archives of Photogrammetry, Remote Sensing and Spatial Information Sciences **35** (B3): 41–45.

ZHANG, L., HE, X., BALZ, T., WEI, X. & LIAO, M., 2011: Rational function modeling for spaceborne SAR datasets. – ISPRS Journal of Photogrammetry and Remote Sensing **66** (1): 133–145.

ZHANG, Z., 1994: Iterative Point Matching for Registration of Free-form Curves and Surfaces. – International Journal of Computer Vision **13** (2): 119–152.

Address of the Author:

M.-Eng., PhD Candidate, DIMITRA VASSILAKI, National Technical University of Athens, School of Rural and Surveying Engineering, Athens, Greece, Tel.: +30-21-0772-2653, Fax: +30-21-0772-2677, e-mail: dimitra.vassilaki@gmail.com